PHILOSOPHICAL TRANSACTIONS A

rsta.royalsocietypublishing.org

Research

Cite this article: Ecke RE, Backhaus S. 2016 Plume dynamics in Hele-Shaw porous media convection. *Phil. Trans. R. Soc. A* **374**: 20150420. http://dx.doi.org/10.1098/rsta.2015.0420

Accepted: 21 July 2016

One contribution of 12 to a theme issue 'Energy and the subsurface'.

Subject Areas:
fluid mechanics, geophysics, hydrology

Keywords:
porous media, convection, plume dynamics

Author for correspondence:
Robert E. Ecke
e-mail: ecke@lanl.gov

THE ROYAL SOCIETY PUBLISHING

Plume dynamics in Hele-Shaw porous media convection

Robert E. Ecke[1] and Scott Backhaus[2]

[1]MPA-CMMS and CNLS, and [2]A-1, Los Alamos National Laboratory, Los Alamos, NM 87545, USA

REE, 0000-0001-7772-5876

Mass transport in multi-species porous media is through molecular diffusion and plume dynamics. Predicting the rate of mass transport has application in determining the efficiency of the storage and sequestration of carbon dioxide. We study a water and propylene–glycol system enclosed in a Hele-Shaw cell with variable permeability that represents a laboratory analogue of the general properties of porous media convection. The interface between the fluids, tracked using an optical shadowgraph technique, is used to determine the mass transport rate, the spatial separation of solutal plumes, and the velocity and width characteristics of those plumes. One finds that the plume dynamics are closely related to the mass transport rate.

This article is part of the themed issue 'Energy and the subsurface'.

1. Introduction

The transport of variable density fluids in a porous medium is an important aspect of understanding and predicting the convective mixing of CO_2 sequestered in deep saline aquifers [1]. When CO_2 is injected into such aquifers, its lower density relative to the brine solution causes it to rise until it is trapped by cap rock structures. In this state, the CO_2 may escape back to the surface and defeat the purpose of the sequestration process. Diffusion of CO_2 into the brine would eventually yield a stable situation but molecular diffusion alone is prohibitively slow, so one needs to consider other processes. Gravitationally driven convection is possible because the density of the brine increases as CO_2 is incorporated across the fluid interface; CO_2 is partially immiscible with respect to the brine. We consider here an analogue system that displays some of the same features of CO_2 sequestration without many of the complications of the real system.

The hydrodynamic instability of two-phase porous media convection is similar to the thickening and instability of thermal layers in thermal convection [2], although in that case the flow rapidly becomes fully nonlinear whereas the porous media allow for a simpler formulation. Analytic calculations and numerical simulations have been performed [3–10] to evaluate the time to instability and the resulting mass transport efficiency. Laboratory experiments, however, have not been able to capture the main features of instability and mass transfer in realistic high-pressure supercritical CO_2 brine systems. Thus, researchers have explored analogue experiments that capture the main features of buoyancy-driven porous media convection [11–15]. Here, we describe details of our analogue approach [13] and concentrate on properties of our system rather than upon justifying the analogy or reviewing other work in this area (see, for example, [16] for an analysis of the limitations of this analogy). Of particular interest in this short report is the theoretical and experimental analysis of Hele-Shaw flows [10,15].

In our earlier work [13], we used the fluid height H as the natural length scale in the problem. Another choice is to use the advection–diffusion balance length scale [10,15], $L = D/U$, where the free fall velocity is given by $U = g(\Delta\rho/\rho)K/\nu$ with acceleration of gravity g, fractional density difference between the two fluids $\Delta\rho/\rho$, porous media permeability K, fluid mass diffusivity D and fluid viscosity ν (the porosity is 1 for Hele-Shaw flow). Using L as the scale of length, one obtains time scale $\tau_L = L/U = D/U^2$. Alternatively, using H for length, one has $\tau_c = H/U$. The time scales are related: $\tau_L = (L/H)\tau_c$. As discussed in [10,15], the Rayleigh number $\mathrm{Ra} = g(\Delta\rho/\rho)KH/(D\nu)$ only becomes important when the plumes reach the bottom, and during the time interval of study mass flux is predicted to be independent of Ra in the ideal two-dimensional limit. We will discuss aspects of these ideas in the context of our velocity and mass transport measurements.

2. Experiment

The experimental apparatus is a Hele-Shaw cell (figure 1*a*) made from two 1.2 cm thick polycarbonate sheets separated by stainless steel shims of thickness b. The lateral dimension of the fluid region is 7.6 cm and the initial height H of the bottom fluid region ranges from 1.2 to 5 cm. The flow in the gap satisfies, to first approximation, Darcy's Law with an isotropic permeability $K = b^2/12$ and a porosity of 1. For our experiments, the values $0.25 < b < 0.48$ mm yield permeabilities in the range $0.54 \times 10^{-4} \leq K \leq 1.94 \times 10^{-4}$ cm^2 (5000–20 000 Darcy). Water with density $\rho_w = 1.000\,\mathrm{g\,cm^{-3}}$ fills the top section of the cell and is initially separated from the lower section fluid, propylene glycol (PPG), with density $\rho_{ppg} = 1.035\,\mathrm{g\,cm^{-3}}$,[1] by two thin metal shims of thickness less than 0.1 mm. A 0.0076 cm thick shutter shim is then removed horizontally from between the two fluids, leaving behind the 0.01 cm thick frame shim to ensure a liquid-tight seal. The shutter shim is removed so as to minimize disturbances of the interface, but occasionally perturbations were observed. These small effects did not influence the flow appreciably for the types of measurements presented here. The removal of the shutter shim opens up a 0.01 cm thick horizontal gap at the interface between the polycarbonate sheets of the upper and lower cells, i.e. at the initial miscible interface between the fluids. Our cell-filling method ensures that this pocket is occupied by water after the shim removal.[2]

As the fluids mix, the resultant mixture, for water mass fraction x between 0% and 50%, has the property of becoming heavier than the pure PPG fluid, i.e. $\rho_x \geq \rho_{ppg}$. After a period of molecular diffusion, the interface becomes gravitationally unstable and solutal plumes are formed. In contrast to a CO_2/brine system, the viscosity and mass diffusivity of the water/PPG system are highly dependent on concentration. When computing experimental parameters or making comparisons with calculations or simulations, we use the transport properties of a 30% water/70% PPG mixture, i.e. $\nu = 0.1\,\mathrm{cm^2\,s^{-1}}$ and (see footnote 1) $D = 1 \times 10^{-6}\,\mathrm{cm^2\,s^{-1}}$ (estimated

[1]Density and dynamic viscosity data for PPG are taken from the manufacturer's data (http://dow-answer. custhelp.com/).

[2]The addenda shim volume produces a delay in the motion of the interface estimated to be of the order of several τ_c.

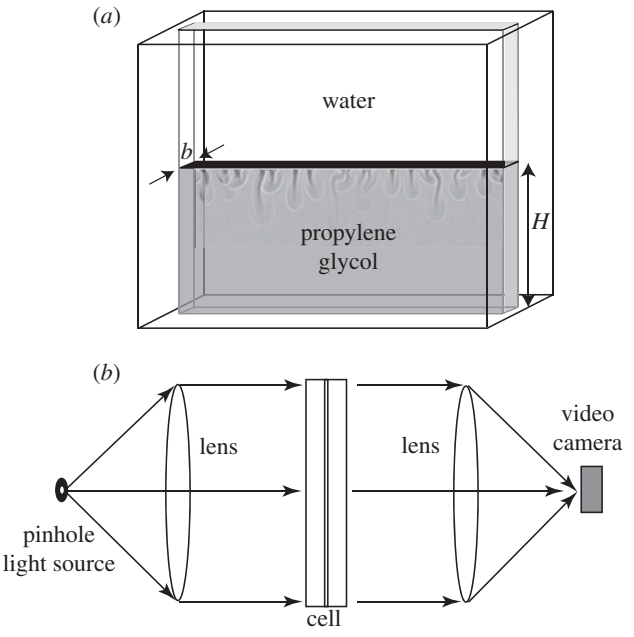

Figure 1. (*a*) Schematic of the Hele-Shaw convection apparatus with width *b* and height *H* indicated. The top fluid is water and the bottom fluid is propylene glycol. The two fluids are separated by a thin metal shim which is withdrawn horizontally to begin an experimental run. (*b*) A side view of the shadowgraph measurement is indicated schematically (not to scale). The sensitivity of the shadowgraph is adjusted by varying the distance from the fluid layer to the focusing lens.

using data from [17]), which corresponds to the mixture of maximum density $\rho = 1.044\,\mathrm{g\,cm^{-3}}$ or the maximum density difference of $\Delta\rho = 0.009\,\mathrm{g\,cm^{-3}}$ relative to the underlying PPG.

The flow is visualized using an optical shadowgraph technique (figure 1*b*) in which the curvature (second derivative) of the index of refraction (proportional to the mixture concentration) of the inhomogeneous fluid mixture causes concentration (brighter) or dispersion (darker) in the optical signal. Although the shadowgraph technique can be made quantitative, here we use it as a qualitative visualization tool. The images resolve an area of lateral size $W = 3.0$ cm and height 2.4 cm with resolutions of 1280×1024 pixels in the horizontal and vertical directions, respectively. Approximately 2000 frames are gathered during each run with a camera frame rate that depends on K: runs at the highest and lowest permeability last 2.5 h and 10 h, respectively. After an initial period in which PPG preferentially diffuses into the water owing to an asymmetric dependence of $D(x)$ [17] (D is larger for PPG diffusing into water than for water diffusing into PPG), the diffusion layer thickens, the influence of buoyancy overcomes lateral diffusion, and hydrodynamic instability occurs as small perturbations in the dense diffusive interface grow into downward moving plumes. Figure 2 shows this evolution of a typical experimental run at various times after initiation. The dashed line and box in figure 2*c* show the horizontal line used to create a space–time plot of the plume dynamics and the region used to zoom in on the motion of a single well-defined plume, respectively.

3. Plume characteristics

The characteristics of the 15 experimental runs are tabulated in table 1. There are three runs for each value of the gap thickness b, which ranges from 0.0254 to 0.0483 cm. The gap b sets the permeability $0.54 \times 10^{-4} < K < 1.94 \times 10^{-4}\,\mathrm{cm^2}$, the convective velocity U, the length scale L, and the time scale τ_L, whereas Ra and τ_c depend on both b and H. We report the velocity of plumes in terms of the scaled velocity $\tilde{v} = v/U$.

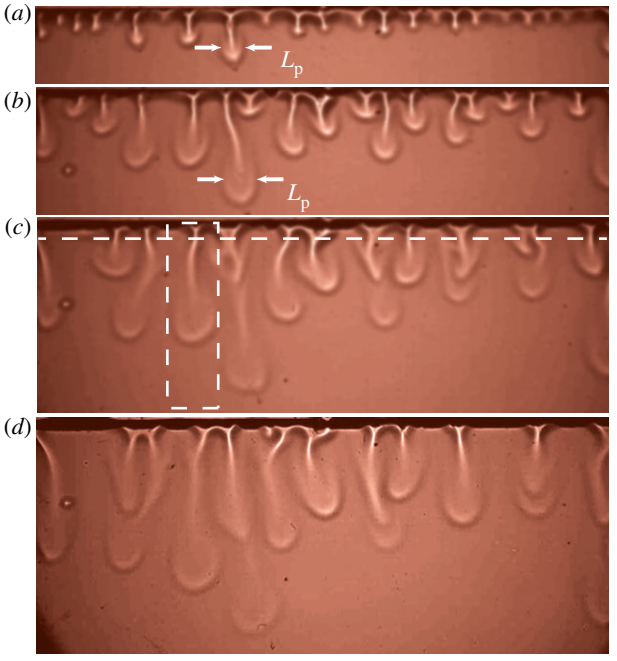

Figure 2. Shadowgraph images (false colour) for t/τ_c: (*a*) 1.0, (*b*) 2.0, (*c*) 3.0 and (*d*) 4.0. Conditions: $U = 0.0046$ cm s^{-1}, $L = 2.2 \times 10^{-4}$ cm $= 2.2$ µm, $H = 2.54$ cm, $\tau_c = 550$ s, $\tau_L = 0.043$ s and Ra $= 11\,700$. Plume width L_p is indicated in (*a*,*b*). Dashed line in (*c*) indicates the line for creating the space–time plot. Dashed box in (*c*) indicates the approximate area for illustrating single plume evolution. (Online version in colour.)

Table 1. Tabulated data for different experimental runs. Gap thickness b, permeability K, bottom fluid height H, convective velocity U, length scale L, convective time τ_c, advection–diffusion time τ_L, Rayleigh number Ra, and average scaled velocity $\langle\tilde{v}\rangle$. Units are indicated.

b (cm)	K (10^{-4} cm^2)	H (cm)	U (cm s^{-1})	L (µm)	τ_c (s)	τ_L (s)	Ra	$\langle\tilde{v}\rangle$
0.0254	0.54	5.08	0.0046	2.2	1100	0.043	23 400	0.059
0.0254		2.54			550		11 700	0.054
0.0254		1.27			275		5800	0.081
0.0305	0.77	5.08	0.0066	1.5	770	0.023	33 300	no data
0.0305		2.54			385		16 700	0.040
0.0305		1.27			193		8300	0.058
0.0356	1.05	5.08	0.0089	1.1	571	0.012	45 500	0.047
0.0356		2.54			286		23 400	0.059
0.0356		1.27			143		11 700	0.054
0.0406	1.38	5.08	0.0118	0.85	430	0.0072	59 700	0.026
0.0406		2.54			215		29 900	0.038
0.0406		1.27			108		14 900	0.037
0.0483	1.94	5.08	0.0165	0.61	308	0.0037	83 100	0.041
0.0483		2.54			154		41 550	0.037
0.0483		1.27			77		20 800	0.072

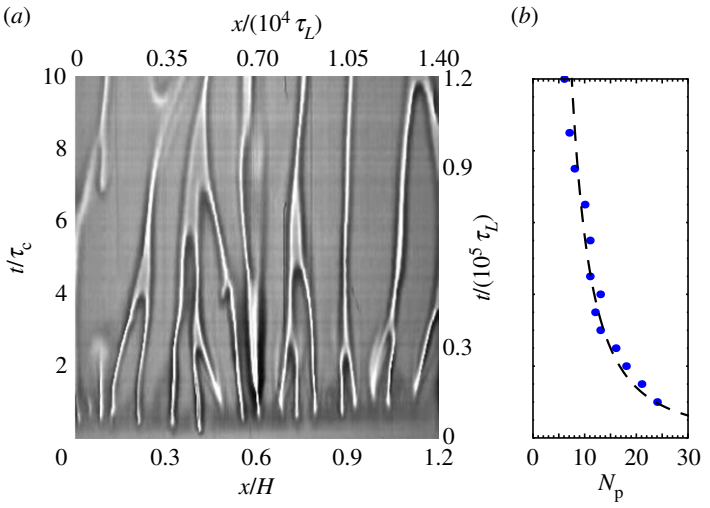

Figure 3. (*a*) Space–time plot with vertical axis t/τ_c (left) or $t/(10^5\tau_L)$ (right) and horizontal axis x/H (bottom) or $t/(10^4\tau_L)$ (top). Conditions as in figure 2. (*b*) Time evolution of the number of plumes N_p at the fluid interface. (Online version in colour.)

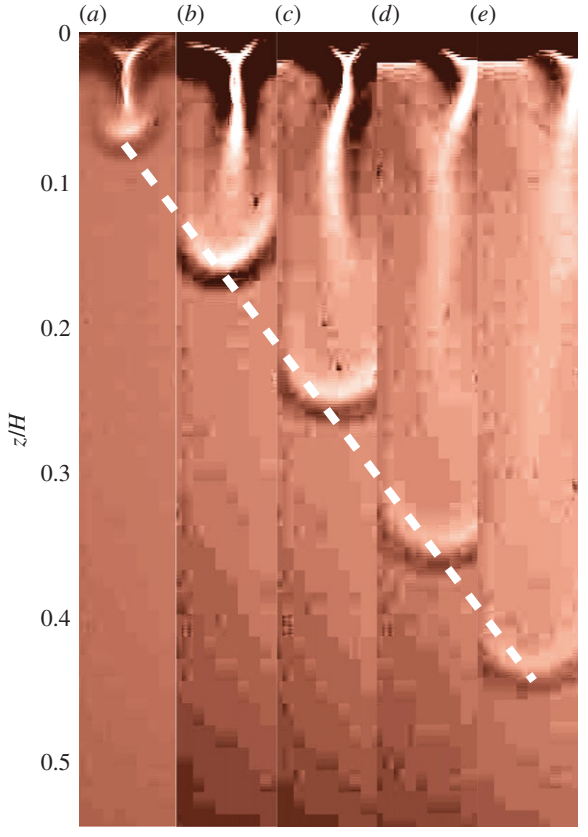

Figure 4. Shadowgraph images (false colour) for t/τ_c: (*a*) 1.0, (*b*) 2.0, (*c*) 3.0, (*d*) 4.0 and (*e*) 5.0. Conditions as for figure 2. Vertical axis is the distance from the initial interface position in units z/H. Dashed line indicates the uniform velocity propagation of a plume as defined by its furthermost position from the initial interface. The first plume encounters undisturbed conditions, whereas the later ones encounter plume interactions and plume renucleation phenomena. (Online version in colour.)

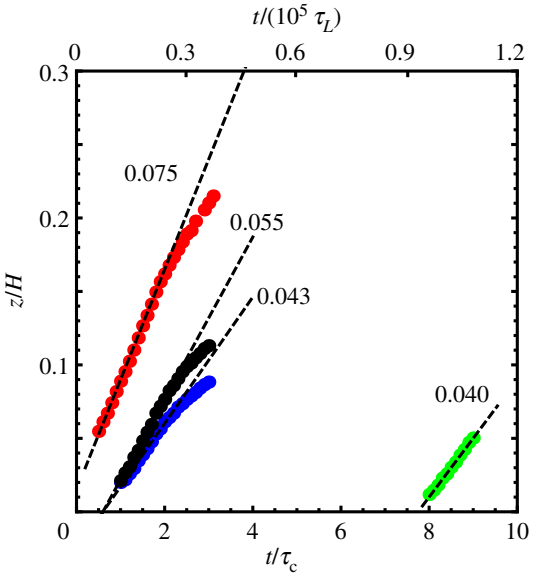

Figure 5. The vertical position z/H versus t/τ_c (bottom axis) or t/τ_L (top axis) for four different plumes in the same run at different times—conditions as for figure 2. The labelled dashed lines indicate constant velocity where the values of $\tilde{v}$ are indicated. At depths of order $z/H \sim 0.1$, the plumes slow slightly as they spread out. (Online version in colour.)

The properties of the solutal plumes that we address here are the lateral plume spacing, the evolution of plume width and the vertical convective velocity. A useful representation of the data are a space–time plot of the dynamics through a horizontal line parallel (figure 2*c*) to the initial interface as shown in figure 3*a*. Time increases upwards and is measured in t/τ_c (left) or t/τ_L (right) increasing upwards, and lateral distance is scaled by H (bottom) or L (top). There are initially a larger number of plumes N_p in the horizontal frame L but the plumes coarsen through merger of nearby plumes [9,10,13,15] before reaching a steady state where the coarsening is balanced by the creation of new plumes at the wider, relatively unperturbed sections of the moving interface. The merger of plumes is shown in figure 3*a* as space–time dislocations—two lines become one. In figure 3*b*, the number of plumes at the interface N_p is shown as a function of scaled time with time increasing upwards. Owing to coarsening that occurs between the interface and the line defining the space–time evolution, the number in the space–time plot is less than N_p.

The vertical plume velocity is determined from video images as the vertical displacement of the plume tip as illustrated in figure 4. The velocity is fairly constant for an individual plume that does not merge, although typically the plume slows as it spreads out. We show some typical trajectories in figure 5 for a single experimental run (same conditions as in figure 2). The first one starts as plumes begin to form, whereas the later ones experience more complex conditions involving plume merger and renucleation (the formation of new plumes in undisturbed sections of the interface). The variety of conditions into which the plumes propagate and the effects of plume interactions suggest the origins of the significant spread in plume velocities.

One final characteristic of the plume dynamics is the plume width L_p as a function of propagation time shown in figure 6. Choosing an initially large plume for conditions with ($b = 0.028$ cm and $\mathrm{Ra} = 11\,700$), we plot the scaled plume width L_p/λ_c (λ_c is the early time pattern wavelength and the width is the full-width half-maximum of the plume profile) versus t/τ_c (bottom axis) and t/τ_L (top axis). There is some uncertainty in this measurement owing to nonlinear distortions in the shadowgraph measurements but the transition to more rapidly widening plumes is associated with the formation of the mushroom-shaped plume head arising from the shear with the slowly upwelling fluid.

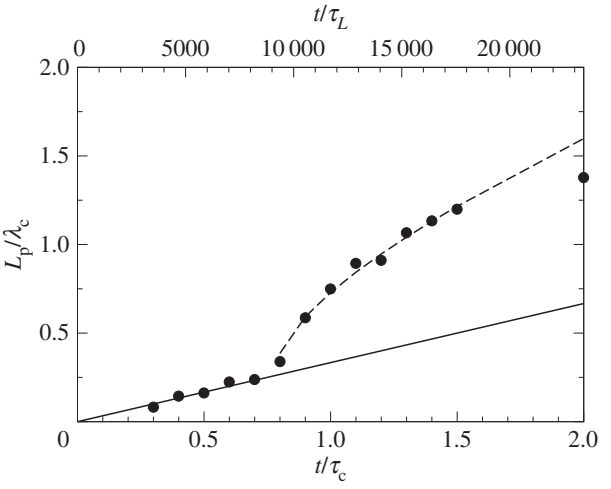

Figure 6. The scaled plume width L_p/λ_c versus scaled time t/τ_c (bottom axis) and t/τ_L (top axis). The solid line is a linear fit at short times $t/\tau_L < 9000$ ($t/\tau_c < 0.75$) and the dashed line is a combined linear (from short times) and square root fit for $t/\tau_L > 9000$ ($t/\tau_c > 0.75$).

(a) Wavelength and coarsening

The plumes coarsen as they grow downwards through the process of merger. This leads to a smaller number of plumes at a later time. Eventually, new plumes are created, which leads to an approximately steady number of plumes per lateral distance. We first consider the wavenumber $k(t) = 2\pi N_p(t)/W$ for a single experimental run in figure 7*a* versus scaled times t/τ_c (bottom) and t/τ_L (top) where there is an initial rapid decrease followed by a gradual equilibration. The total number at long time is $N_p \approx 6$ ($k \approx 12$) with fluctuations of ± 1, i.e. of order 10%. The evolution of k is complicated with various regions of behaviour such that a single function is unlikely to capture the dynamics. Nevertheless, an exponential function captures the general trend: $k = 11 + 60\,e^{-(t/\tau_c)/2.0}$ (the corresponding characteristic time when scaling by τ_L is about 64 000). When all the different runs are concatenated together (figure 7*b*), one obtains a similar result with an overall trend consistent with $k = 13 + 60\,e^{-(t/\tau_c)/3.5}$. Thus, the overall coarsening process seems to be consistent with a characteristic coarsening time of about 2.7 τ_c with little dependence on H (and thereby on Ra). If one collapses the curves by scaling with τ_L as in figure 7*c*, one gets better collapse (less lateral spread) at early times $t/\tau_L < 10\,000$ but larger variation at intermediate times $10\,000 < t/\tau_L < 800\,000$. This is consistent with the idea that the flow does not feel the bottom for early times, of order 20 τ_c (time for a plume to reach the bottom is $H/\tilde{v} \approx 20\tau_c$—see below).

(b) Velocity statistics

Individual plume velocities are obtained from the images of the evolving plume dynamics as illustrated in figure 2. An emphasis is on plumes that are well separated from others and on early times although a fraction are for conditions where strong mergers and renucleation phenomena occur. For each experimental run, the average of about 50 plumes was measured (there was only one run per set of experimental conditions). Several examples are shown in figure 4 with scaled displacements (units of H) versus scaled time t/τ_c. We present the velocity scaled by U, $\tilde{v} = v/U$. One has a roughly constant slope for a time interval of order τ_c, after which plumes tend to slow slightly. The mean velocity $\langle\tilde{v}\rangle$ is weakly dependent on Ra number as shown in figure 8, following $1.2\mathrm{Ra}^{-0.33}$, and the standard deviation $\sigma_{\tilde{v}}$ has the same dependence on Ra but with a smaller constant coefficient $0.45\mathrm{Ra}^{-0.33}$. In other words, one has $\sigma_{\tilde{v}}/\langle\tilde{v}\rangle \approx 0.38$.

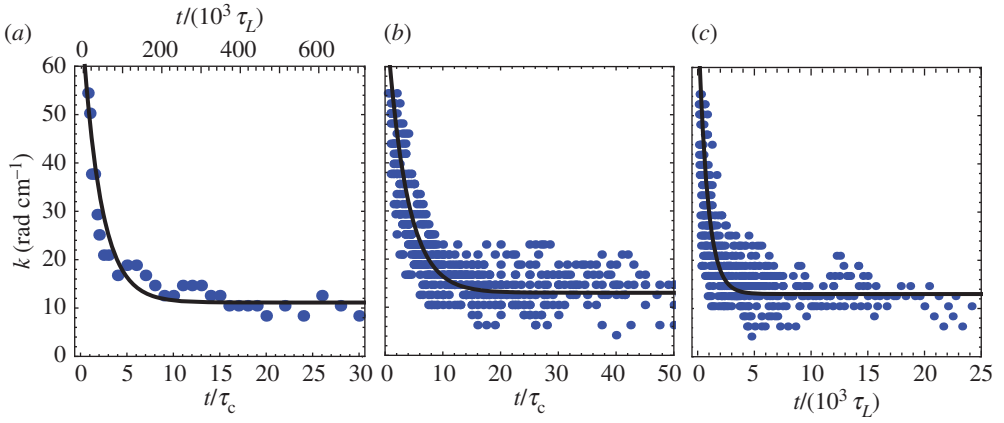

Figure 7. Plume wavenumber k versus scaled time. (*a*) Single experimental run ($b = 0.0254$ cm, Ra $= 23\,400$); solid line is $11 + 60\,\mathrm{e}^{-t/(2.0\tau_c)}$. Bottom axis is scaled t/τ_c and top axis is scaled $t/(10^3\,\tau_L)$. (*b*) All runs using scaled t/τ_c. Solid line is $13 + 60\,\mathrm{e}^{-t/(3.5\tau_c)}$. (*c*) All runs using scaled t/τ_L; solid line is $13 + 60\,\mathrm{e}^{-t/(8\times10^4\tau_L)}$. (Online version in colour.)

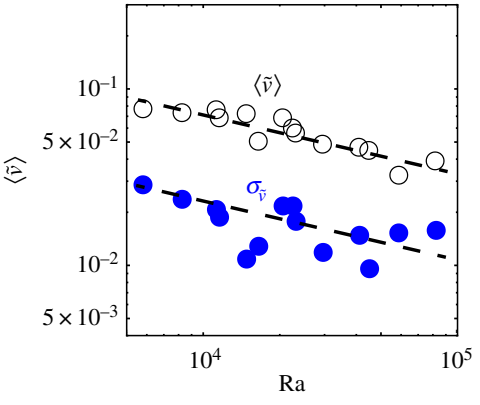

Figure 8. Plume velocity: mean $\langle\tilde{v}\rangle$ and standard deviation $\sigma_{\tilde{v}}$ versus Ra. Dashed lines are $1.2\mathrm{Ra}^{-0.33}$ and $0.45\mathrm{Ra}^{-0.33}$ for mean and standard deviation. (Online version in colour.)

If one computes the probability distribution function (PDF), where one subtracts the mean and divides by the standard deviation, i.e. $v^* = (\tilde{v} - \langle\tilde{v}\rangle)/\sigma_{\tilde{v}}$, one obtains the PDF for all the data as presented in figure 9, which has Gaussian form and unit width. There is possibly a bit of negative skewness to the distribution, indicating an enhanced tendency for the plumes to slow down as in figure 5. The mean value of the plume velocity is roughly consistent with the numerical simulation value for two-dimensional porous media solutal convection at a rigid horizontal interface of 0.1 [10] although our values are somewhat less, in the range $0.03 < \langle\tilde{v}\rangle < 0.09$.

4. Mass transport

The plume dynamics evolve to produce a steady-state mass flux across the two-fluid interface in which the action of the plumes scours the interface keeping it, on average, of uniform thickness. Relative to the standard conditions of Rayleigh–Bénard convection where there is a fixed horizontal boundary, the boundary conditions for either a miscible or immiscible interface allow the interface to distort. This distortion results in enhanced mass transport relative to a flat interface [9,16]. The steady flux regime represents the balance of plume transport and merger with

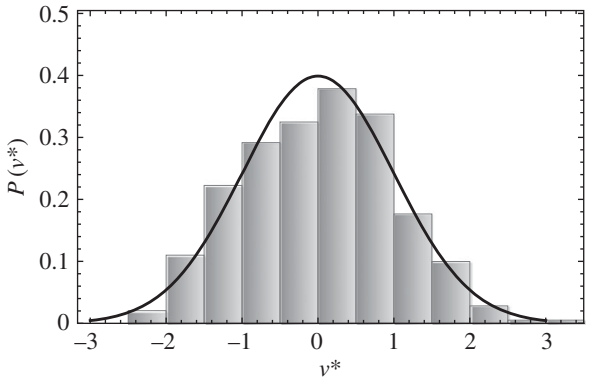

Figure 9. Probability distribution $P(v^*)$. Solid curve is Gaussian with zero mean and unit standard deviation.

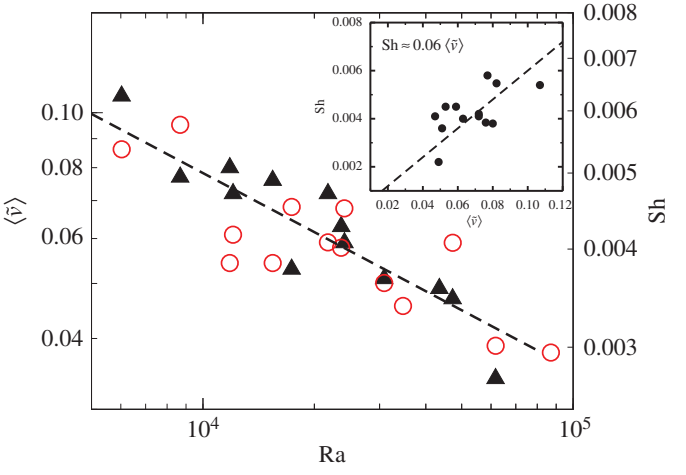

Figure 10. $\langle\tilde{v}\rangle$ (left axis, solid triangles) and Sh (right axis, open circles) versus Ra. Dashed line is $0.05\mathrm{Ra}^{-0.25}$ consistent with the Sh data. Inset shows Sh versus $\langle\tilde{v}\rangle$. (Online version in colour.)

the nucleation of new plumes in the boundary-layer regime between major plumes [9,10,13,15]. From numerical simulations [10], one gets a constant dimensionless mass transport of $\mathrm{Sh} = 0.017$ (note that the Nusselt number, the ratio of the mass flux to the steady state, i.e. linear profile, diffusive mass flux across a height H is related to Sh by $\mathrm{Nu} = \mathrm{Sh}\,\mathrm{Ra}$), whereas the results for our PPG/water system show a weak Ra dependence: $0.045\mathrm{Ra}^{-0.24}$. For $\mathrm{Ra} = 10^4$, one has $\mathrm{Sh} = 0.0045$ and a total range $0.003 < \mathrm{Sh} < 0.006$. The correspondence between the mass transport and the average plume velocity is shown in figure 10. The dependence on Ra is about the same with $\mathrm{Sh} \approx 0.06\langle\tilde{v}\rangle$. The variation with Ra is approximately $\mathrm{Ra}^{0.25}$ (the difference between the $-1/3$ power for the mean velocity and the $-1/4$ power for Sh is within the uncertainty of the data). From the perspective of CO_2 sequestration, mass transport in miscible interfaces with non-monotonic density dependence for the water/PPG may be slightly less than for the partially miscible CO_2 system [16].

5. Conclusion

The analogue system of porous media using PPG and water [13] yields a simple system to quantitatively probe properties of mass transport resulting from solutal plumes. Using shadowgraph imaging, we have characterized the plume dynamics and mass transport of single

interface solutal convection. In particular, the rapid decrease and approach to a steady state of the pattern wavenumber k is collapsed well using either τ_c or τ_L to scale time although the latter is slightly better at earlier times. The measured plume velocities are consistent with the mass transport measurements with the variability of plume velocities arising primarily from the merger and renucleation process. Both the mass transport and plume velocity data show a weak Ra dependence. These results are slightly different from the strictly two-dimensional simulations [10], perhaps pointing to quantitative issues such as the miscible versus partially immiscible interface or the horizontal versus deformable interface [16]. A further difference may arise from the larger impact of Taylor dispersion, which is not negligible for our set-up (see discussion in [15]).

Nevertheless, these analogue systems have proved useful in visualizing plume dynamics and in stimulating more quantitative simulations and better understanding of the limitations of such approaches to the CO_2/brine mixing that underpins attempts at sequestering large quantities of CO_2. The real system is, of course, three-dimensional and measurements of the three-dimensional version of these results will be presented elsewhere.

Authors' contributions. S.B. designed the study and carried out the experiments. R.E.E. performed the data analysis and drafted the manuscript. Both authors read and approved the manuscript.

Competing interests. The authors declare that they have no competing interests.

Funding. This work was carried out under the auspices of the National Nuclear Security Administration of the US Department of Energy at Los Alamos National Laboratory under contract no. DE-AC52-06NA25396.

Acknowledgements. We acknowledge useful conversations with C. Doering.

References

1. Metz D, Davidson O, de Coninck H, Loos M, Meyer L. 2005 *IPCC special report on carbon dioxide capture and storage*, ch. 5. New York, NY: Cambridge University Press. (Prepared by Working Group III of the Intergovernmental Panel on Climate Change.)
2. Foster TD. 1965 Stability of a homogeneous fluid cooled uniformly from above. *Phys. Fluids* **8**, 1249–1257. (doi:10.1063/1.1761393)
3. Ennis-King J, Preston I, Paterson L. 2005 Onset of convection in anisotropic porous media subject to a rapid change in boundary conditions. *Phys. Fluids* **17**, 084107. (doi:10.1063/1.2033911)
4. Xu X, Chen S, Zhang D. 2006 Convective stability analysis of the long-term storage of carbon dioxide in deep saline aquifers. *Adv. Water Resour.* **29**, 397–407. (doi:10.1016/j.advwatres.2005.05.008)
5. Riaz A, Hesse M, Tchelepi HA, Orr FM. 2006 Onset of convection in a gravitationally unstable diffusive boundary layer in porous media. *J. Fluid Mech.* **548**, 87–111. (doi:10.1017/S0022112005007494)
6. Ennis-King J, Paterson L. 2007 Coupling of geochemical reactions and convective mixing in the long-term geological storage of carbon dioxide. *Int. J. Greenhouse Gas Control* **1**, 86–93. (doi:10.1016/S1750-5836(07)00034-5)
7. Rapaka S, Chen S, Pawar RJ, Stauffer PH, Zhang D. 2008 Non-modal growth of perturbations in density-driven convection in porous media. *J. Fluid Mech.* **609**, 285–303. (doi:10.1017/S0022112008002607)
8. Rapaka S, Pawar RJ, Stauffer PH, Zhang D, Chen S. 2009 Onset of convection over a transient base-state in anisotropic and layered porous media. *J. Fluid Mech.* **641**, 227–244. (doi:10.1017/S0022112009991479)
9. Hewitt DR, Neufeld JA, Lister JR. 2013 Convective shutdown in a porous medium at high Rayleigh number. *J. Fluid Mech.* **719**, 551–586. (doi:10.1017/jfm.2013.23)
10. Slim AC. 2014 Solutal-convection regimes in a two-dimensional porous medium. *J. Fluid Mech.* **741**, 461–491. (doi:10.1017/jfm.2013.673)
11. Backhaus S. 2010 Laboratory measurements of large-scale carbon sequestration flows in saline reservoirs. In *Ninth Annual Conf. on Carbon Capture and Sequestration, Pittsburgh, PA, 10–13 May 2010*. Washington, DC, USA: Exchange Monitor Publications and Forums.

12. Neufeld JA, Hesse MA, Riaz A, Hallworth MA, Tchelepi HA, Huppert HE. 2004 Convective dissolution of carbon dioxide in saline aquifers. *J. Fluid Mech.* **500**, 263–281. (doi:10.1017/S0022112003007298)
13. Backhaus S, Turitsyn K, Ecke RE. 2011 Convective instability and mass transport of diffusion layers in a Hele-Shaw geometry. *Adv. Water Resour.* **106**, 104501. (doi:10.1103/physrevlett.106.104501)
14. Hidalgo J, Fe J, Cuetao-Felgueroso L, Juanes R. 2012 Scaling of convective mixing in porous media. *Phys. Rev. Lett.* **109**, 264503. (doi:10.1103/PhysRevLett.109.264503)
15. Slim AC, Bandi MM, Miller JC, Mahadevan L. 2013 Dissolution-driven convection in a Hele-Shaw cell. *Phys. Fluids* **25**, 024101. (doi:10.1063/1.4790511)
16. Raad SMJ, Hassanzadeh H. 2015 Onset of dissolution-driven instabilities in fluids with non monotonic density profile. *Phys. Rev. E* **92**, 053023. (doi:10.1103/PhysRevE.92.053023)
17. Hubel A, Bidault N, Hammer B. 2002 Transport characteristics of glycerol and propylene glycol in an engineered dermal replacement. In *Proc. ASME 2002 Int. Mechanical Engineering Congress and Exposition, New Orleans, LA, 17–22 November 2002*, pp. 121–122. New York, NY: American Society of Mechanical Engineers.